Giant Stark Effect in Two-Dimensional Hittorf's Phosphorene

Ju Zhou, Tian-Yi Cai,[*] and Sheng Ju[†]

Department of Physics, Soochow University, Suzhou 215006, P. R. China

The electric field tunable band gap and optical properties in low-dimensional materials (quantum-confined Stark effect) are very useful in applications of optoelectronics. In this paper, based on the many-body perturbation method, we investigate the evolution of the quasiparticle electronic structure, exciton, and optical properties of two-dimensional (2D) Hittorf's phosphorene under an out-of-plane electric field. Compared to other 2D monolayers, the relatively large thickness of Hittorf's phosphorene leads to a significant reduction in the quasiparticle band gap when an electric field is applied along the quantum confinement direction. The unique bilayer structure, on the other hand, guarantees a well spatial separation of photon-excited electron-hole pairs and, consequently, reduced exciton binding energy under an out-of-plane electric field. These combined effects lead to an almost fixed exciton energy and optical absorption edge at low applied electric fields. However, when the field is larger than 0.1 V/Å, substantial reductions in the exciton energy and optical absorption edge are identified. For the higher-order exciton states, the involvement of more complex band-to-band electron-hole pair formation results in a nonmonotonic electric field dependence. The effective optical modulation accompanied with these giant Stark effects shows potential applications of Hittorf's phosphorene in 2D optoelectronic devices.

I. INTRODUCTION

Two-dimensional (2D) materials have attracted wide interest in condensed matter physics and material science. From gapless graphene to narrow-band-gap black phosphorene, intermediate-band-gap transition metal dichalcogenides (TMDs), and wide-band-gap semiconductors [e.g., blue phosphorene, Hittorf's phosphorene, III-VI monochalcogenides, graphane, C_3N/C_3B, and boron nitride (BN)], 2D materials could cover a wide range of the optical spectrum. Enhanced electron-hole interaction, i.e., excitonic effect, in these atomically thin layers will lead to strong light-matter interactions, making them useful in applications of 2D photodetectors, photovoltaics, and light-emitting diodes (LEDs), etc [1–37].

Among these 2D materials, black phosphorene with a narrow band gap of 2.1 eV has attracted intense interest for its obvious anisotropic optical responses, with a 1.6 eV difference in the optical absorption edge between the polarization along the zigzag and armchair directions of the 2D puckered structure [20–28]. Importantly, as revealed by Qiu *et al.* [27], such anisotropy is intrinsic and independent of the layer thickness and environment screening, showing robust application in optoelectronic devices. In contrast to black phosphorene, another kind of 2D buckled phosphorus hexagonal crystal structure was found to exhibit

a much larger band gap of 3.41 eV with the first exciton state located at 2.85 eV [29]. Although the intrinsic indirect band gap in this buckled monolayer (blue phosphorene) will prohibit its direct applications in optoelectronics as an efficient LED, the unusual strain dependence of the quasiparticle electronic structure and excitonic properties will find advantages in the realization of a funnel structure for the applications of green and blue LEDs [29]. On the other hand, violet (or Hittorf's) phosphorus with a fibrous and layered crystal structure is another wide-band-gap semiconductor [31]. Recently, under ambient conditions, the monolayer of violet (or Hittorf's) phosphorus was isolated experimentally with both mechanical and solution exfoliation methods [32,33]. In particular, the high quality of the solution exfoliated sample paves the solid foundation for further exploration of its physical and chemical properties. Our *ab initio GW* calculations showed that its monolayer has a direct band gap of 3.32 eV [34]. Despite a relatively large thickness of around 10 Å, the optical spectrum is still dominated by exciton effects. The first exciton state is located at 2.41 eV with a strong binding energy of 0.91 eV [34], agreeing with experimental findings of the optical absorption edge of 2.27 eV [33]. Furthermore, polarization-direction-dependent electron-hole excitations have been revealed in this 2D material [34].

The effect of the electric field on the electronic and optical properties of solids has been studied for a long time [38–40]. The Stark effect is one such phenomena where an external electric field is used to perturb the electronic

---

[*]caitianyi@suda.edu.cn

[†]jusheng@suda.edu.cn

structure of the active material and usually provides a shift of the emission line to the lower energies due to a reduction in the band gap. For low-dimensional materials, the electric field could give rise to an obvious change of the energies of quantum states, i.e., the quantum-confined Stark effect (QCSE) [41–70]. The electric field in these cases is applied along the confinement direction of a quantum well or other nanostructure, thereby allowing a large electric field resulting in a giant shift of exciton states and optical properties. As demonstrated in Fig. 1, for 2D materials, the overall exciton energy shift has two components [64]. A reduction in the band gap arises from the opposite movement in energy of the constituent electron states in the conduction bands and the hole states in the valence bands and the magnitude is quadratic on the electric field. The other component of the Stark shift, which is the suppression of the exciton binding energy, results from the opposite motion of the wave function of the constituent electron and hole within the confined structure when an electric field is applied. For a square well, within second-order perturbation theory, such an effect is proportional to t^4, where t is the quantum well thickness [64]. Thus, in typical quantum wells with width extending up to several nanometers, the quadratic reduction in the band gap significantly dominates over the reduction in the exciton binding energy, and thus a shift in the optical spectrum to higher energies is seldom observed. In 2D materials, the dependence of the exciton energy with respect to the electric field could be described as

$$E = -\alpha_1 \times F - \alpha_2 \times F^2 + E_0, \qquad (1)$$

where α_1 is the exciton dipole moment, α_2 is the exciton polarizability, and E_0 is the band gap at $F = 0$ V/Å. For most 2D materials, the thickness of the monolayer is less than 5 Å. The reduction in the band gap under an out-of-plane electric field is extremely small. For example, when the electric field reaches as high as 0.1 V/Å, our theoretical calculated band-gap reduction is very small for some 2D materials, as listed in Table I. However, for Hittorf's phosphorene, the reduction in the band gap could reach as high as 22 meV. Therefore, Hittorf's phosphorene could provide a platform to realize giant QCSE. In this paper, based on the more accurate *GW*-BSE (where BSE refers to the Bethe-Salpeter equation) method, we study the evolution of the quasiparticle band gap, exciton, and optical properties of 2D Hittorf's phosphorene under an out-of-plane electric field. The unusual two-sublayer crystal structure with a relatively large thickness (10.06 Å) could give rise to an obvious reduction in the band gap as well as a spatial separation of electron-hole pairs, and, consequently, significant effects of the electric field on the excitonic properties. Indeed, as we have found, the quasiparticle band gap could decrease by as much as 17 meV under 0.1 V/Å. This value is even larger at 64 meV
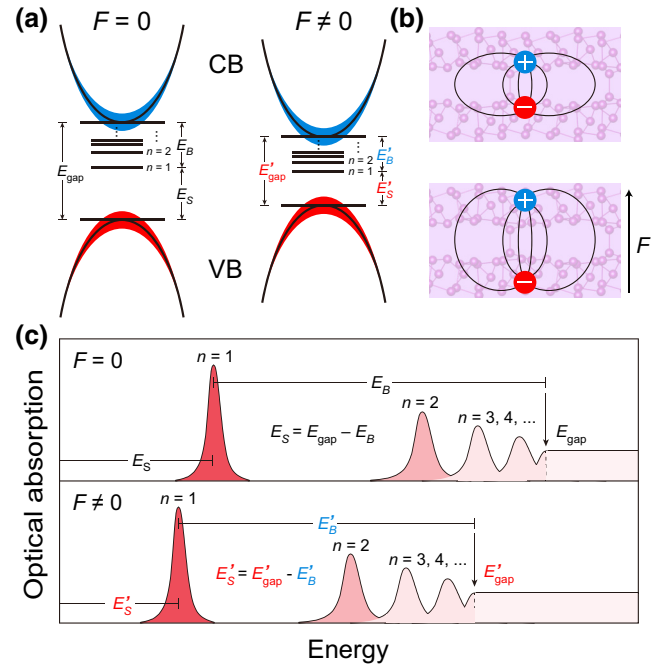

FIG. 1. (a) Schematic illustration of the band structure and the exciton states of a 2D material under an applied electric field. (b) Schematic illustration of the exciton in Hittorf's phosphorene with two sublayers. The electric field strongly modulates the interaction between the electron and the hole, moving them apart and suppressing the binding energy. (c) Schematic illustration of the optical absorption of a 2D material, including a series of exciton states within the quasiparticle band gap. The reduction of the band gap E_{gap} and the reduction of exciton binding energy E_B under an electric field will lead to a shift in the optical absorption to a low energy and a high energy, respectively, therefore modulating the optical band gap E_S as $E_S = E_{gap} - E_B$.

under 0.2 V/Å. In the meantime, a sizeable reduction in the exciton binding energy of 48 meV under such a mediate electric field is found and the overall exciton energy shows a stable reduction of 16 meV at 0.2 V/Å and could reach as high as 56 meV at 0.3 V/Å. We also reveal that the macroscopic dielectric screening in fact changes little with electric fields, and that the electric-field-driven spatial separation and localization of electron and hole wave functions near the band edges with enhanced effective mass play an important role. Our studies have not only provided a deeper understanding of QCSE of excited states in 2D materials, but also shown that the effective modulation of optical absorption in 2D Hittorf's phosphorene under an electric field could find applications in 2D optoelectronics, e.g., electro-optical modulators, electrically tunable and sensitive light-emitting systems.

II. COMPUTATIONAL METHOD

Our first-principle calculations are performed using density-functional theory (DFT) as implemented in the

TABLE I.   The calculated band-gap reduction (based on PBE) of Hittorf's phosphorene, black phosphorene, MoS_2, blue phosphorene, and BN under an applied out-of-plane electric field of 0.1 V/Å.

	Hittorf's phosphorene	Black phosphorene	MoS_2	Blue phosphorene	BN
ΔE (meV)	22	0.37	0.03	0.04	0.04

Quantum Espresso package [71]. Generalized gradient approximations with Perdew-Burke-Ernzerhof (PBE) of norm-conserving pseudopotentials with a plane-wave cutoff of 60 Ry are used [72,73]. The ground-state wave functions and eigenvalues are calculated with a k grid of $6 \times 6 \times 1$. The structures are relaxed until the total forces are less than 0.01 eV/Å and the convergence criterion for total energies is set to 10^{-5} eV. The quasiparticle band structures, exciton, and optical properties are calculated with the BerkeleyGW package [74–76]. A slab model is used with a vacuum layer of 20 Å along the out-of-plane direction. A perpendicular sawtoothlike potential with dipole correction is adopted to simulate the external out-of-plane electric field with a magnitude up to 0.3 V/Å. In the meantime, a truncated Coulomb interaction between Hittorf's phosphorene and its periodic image is adopted for the excited-state calculations (both quasiparticle and excitonic properties) [77]. For the convergence of quasiparticle energies [78], we have tested dependence on the k-grid size, number of bands, as well as the dielectric cutoff. We use a coarse k grid of $6 \times 6 \times 1$, empty bands of 30 times more than the valence bands, and a dielectric cutoff of 10 Ry [34]. For the BSE part, a fine k grid of $36 \times 36 \times 1$ is used [34]. It is noted that fine sampling is necessary to capture fast variation in screening at small wave vectors and fine features in exciton wave functions, which are tightly localized in k space. We use a Gaussian smearing with a broadening constant of 5 meV in the optical absorbance spectrum. The number of bands for optical transitions is eight for both valence and conduction bands, which is sufficient to cover the span of visible light. The exciton lifetime is calculated based on Fermi's golden rule [79,80]. The detailed computational framework is shown in Appendix A.

III. RESULTS AND DISCUSSION

A. Evolution of the quasiparticle electronic structure and optical properties in Hittorf's phosphorene under an out-of-plane electric field

The atomic crystal structure of Hittorf's phosphorene is presented in Fig. 2. The monolayer structure has two sublayers that are composed of phosphorous tubes with pentagonal cross section. These tubes are covalently bonded to the tubes orthogonally in the other sublayer. The optimized in-plane lattice constants of Hittorf's phosphorene are $a = 9.24$ Å and $b = 9.26$ Å, and there is a twofold rotation symmetry along the x axis with point group C_2 [34] (see the detailed atomic positions in Appendix B). The electric field is applied perpendicularly to the x-y plane and along the z direction.

To investigate the effect of the external electric field, the electrostatic potential of Hittorf's phosphorene is presented in Fig. 3(a). Within the material stuff (10 Å $< z <$ 20 Å), the difference upon application of electric fields is small. The effective electric field distribution along the z axis is obtained as

$$\mathcal{F} = -\frac{d(\Delta U)}{dz}, \qquad (2)$$

where ΔU is the electrostatic potential difference upon the application of the electric field, as shown in Fig. 3(b). The potential drop between the upper and lower surfaces is 0.45 V for an electric field of 0.3 V/Å, indicating the effective screening of the external electric field in Hittorf's phosphorene. By differentiating the ΔU, the effective electric field is obtained and presented in Fig. 3(c). In the vacuum region, the calculated electric field $\mathcal{F}$ is nearly constant, equal to the applied value. Deep in the two sublayers, $\mathcal{F}$ is about 5% of the applied value. The maximal effective $\mathcal{F}$ is found at the interface between the two sublayers. The charge density difference compared to the zero-bias condition is presented in Fig. 4. When an electric field of 0.1 V/Å is applied, few electrons flow from the upper sublayer to the lower sublayer. With increasing field strength, the electrons accumulate at the lower part of both sublayers. This finding shows that, under high electric fields, a much stronger charge redistribution occurs as the two sublayers in Hittorf's phosphorene behave independently.

The evolution of the quasiparticle band structure of Hittorf's phosphorene under an applied electric field is presented in Fig. 5. The band gap of Hittorf's phosphorene is 3.32 eV (X point) at zero bias. With increasing external electric field, the band gap at the X point decreases to 3.19 eV for 0.3 V/Å. The direct band-gap nature of Hittorf's phosphorene remains until the electric field increases to 0.3 V/Å, where the system evolves into an indirect-band-gap semiconductor with the top of the valence band located at the Γ point. In the meantime, the band dispersion gets flatter when the electric field is applied gradually. The band structure obtained within PBE is shown in Appendix C, where the reduction in the band gap is a little larger than that obtained within the G_0W_0 framework.

The charge redistribution under an applied electric field is reexamined using plots of partial charges. In Fig. 6, we show the states near band edges of the valence band (VB) and the conduction band (CB) at several high-symmetry k points, i.e., Γ, X, M, and Y. At zero bias, electrons are
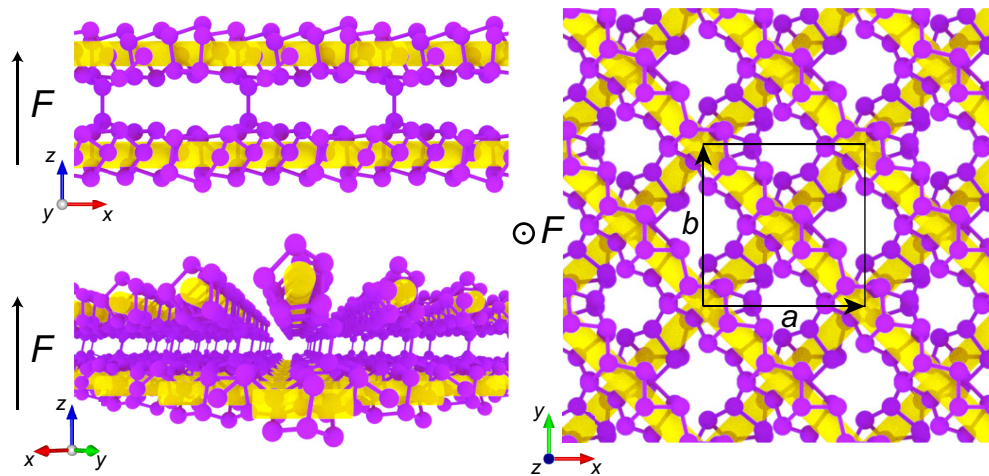
FIG. 2. Illustration of Hittorf's phosphorene under a perpendicular out-of-plane electric field (along the z direction). We show the side view in the left panel and the top view in the right panel. The yellow tubes are added as guides to the eye only to emphasize the fibrous nature of Hittorf's phosphorene.

distributed equally between the two sublayers. The holes, on the other hand, are mainly concentrated in the interlayer space. After applying an out-of-plane electric field, we find that electrons and holes are gradually driven towards the opposite direction in the neighboring sublayers. This is more obvious for the charges at the Γ, Y, and M points (in comparison to the X point), where the direct band gaps are larger. Such evolution of electron orbitals at the band edges is essential to understanding the change of exciton formation and the corresponding optical properties with an electric field.

The lowest direct transition energy from valence to conduction bands in the Brillouin zone is presented in Fig. 7. The valley at the X point is found in all cases. However, when the electric field is applied, the overall direct transition energies are decreased and the valley gets smoothed. Together with the broken twofold rotation symmetry, dramatic changes in the formation of excitons in Hittorf's phosphorene under an out-of-plane electric field could be expected.

The optical absorption spectra for light polarized along the x and y axes of monolayer Hittorf's phosphorene are presented in Fig. 8. At zero bias, the first absorption peak for the light polarized along the x axis is located at 2.41 eV. A detectable decrease of up to 2.35 eV is found when the electric field increases to 0.3 V/Å. The absolute absorbance also shows an obvious decrease. In contrast, when the excitonic effect is not considered (without including electron-hole interaction), the optical absorbance spectrum is continuous (see Appendix D). The absorption edge obtained in this way is much larger than the experimental finding [33]. In the meantime, similar to previous findings in other 2D materials [81,82], the absorption edge moves to the lower energies as long as the electric field is present.

Because of the anisotropic crystal structure, the absorption edges for light polarized along two orthogonal directions are different, with an anisotropy of around 0.06 eV [34]. When applying electric fields, the anisotropy looks increased. The polarization-dependent oscillator strength of the first two exciton states is presented in Figs. 9 and 10, respectively. It is clear that two sets of excitons exhibit strong linear dichroism. We also observe that the polarization angles corresponding to the maximum oscillator strength gradually deviate from the x axis when an electric field is applied. This is attributed to the symmetry breaking between the two sublayers. For the second exciton shown in Fig. 10, the magnitude increases first and decreases rapidly afterwards. As explained later, this behavior is due to the involvement of more complex band-to-band optical transitions during the formation of this exciton state.

By now, we could summarize the dependence of the band gap and optical gap with respect to the electric field. Following the description in Eq. (1), we can obtain the polarizability α_2 associated with the reduction of either the band gap or optical gap of Hittorf's phosphorene. The fittings are shown in Figs. 11 and 12. Here, the intrinsic dipole moment for Hittorf's phosphorene is zero. Therefore, the field dependence is quadratic as $1/F^2$. The polarizability α_2 is then fitted to be 7.2×10^{-10} Dm/V for the quasiparticle band gap and 2.7×10^{-10} Dm/V for the optical gap. Within PBE, α_2 associated with the band-gap reduction is 8.4×10^{-10} Dm/V (see the details in Appendix E). For the band gap at other high-symmetry k points, the evolution shows a similar electric field dependence and detailed data are summarized in Table II. We have also compared our revealed QCSE in Hittorf's phosphorene with other 2D monolayers. By now, many measurements in TMDs have been performed, as summarized in Table III [50,55,60,61,64]. However, accurate
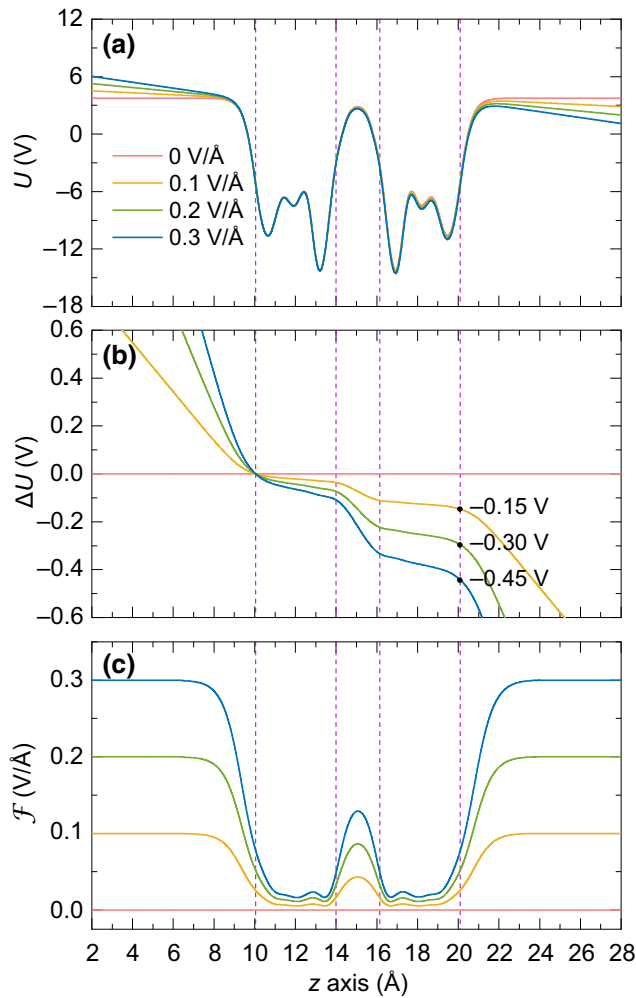
FIG. 3. (a) Evolution of the electrostatic potential profile across Hittorf's phosphorene along the z axis with increasing electric field. The vertical dashed lines indicate the top and bottom boundaries of the two sublayers. (b) The electrostatic potential difference with increasing electric field along the z axis. (c) The calculated effective electric field distribution along the z axis.
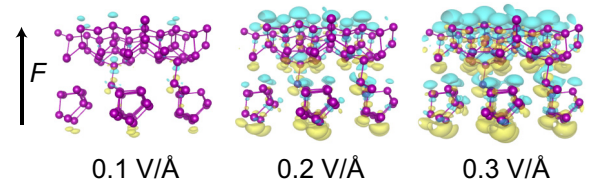

FIG. 4. The charge density difference in comparison with the zero-bias condition. The charge accumulation and depletion are represented by yellow and cyan regions, respectively.

(h-BN) and determined their out-of-plane polarizability to be 7.8×10^{-10} Dm/V, which is an order of magnitude smaller than the estimation in the initial work [50]. Unlike free excitons, localized excitons in encapsulated monolayer WSe$_2$ have shown larger shifts even at low fields, apparently due to their local permanent dipole moment. The polarizability of free exciton species in monolayer TMDs remains a curious problem, especially in the high field regime where polarizability is saturated and quadratic shifts are no longer expected. Recently, Verzhbitskiy *et al.* [60] experimentally studied the out-of-plane polarizability of excitons in the h-BN-encapsulated monolayer WSe$_2$ in strong electric fields of up to 1.6 V/nm (16 MV/cm). They monitored free exciton photoluminescence peaks with increasing electric fields at a constant carrier density, carefully compensating for unintentional photodoping in their double-gated device at 4 K. It was shown that the Stark shift is smaller than 0.4 meV despite the large electric fields applied, yielding an upper limit of polarizability to be 10^{-11} Dm/V [60]. Such an intrinsic small polarizability, which is nearly 2 orders of magnitude smaller than the previously reported value for MoS$_2$ [55], indicates strong atomic confinement of electrons in this 2D system and highlights the unusual robustness of free excitons against

measurement of the Stark shift in monolayer TMDs is challenging due to the intrinsically small polarizability, which is often masked by the strong shift arising from charge modulation effects [54]. A high-quality interface is therefore crucial in minimizing trapping of photocarriers that will lead to unintentional photodoping (or photogating) and a corresponding apparent field-induced shift. In a pioneering experiment, Klein *et al.* [50] revealed a very large polarizability of the order 10^{-8} Dm/V. Later Roch *et al.* [55] addressed this issue by identifying the bias window within which photodoping did not occur and limiting the electric field to below 0.17 V/nm (1.7 MV/cm) to observe the Stark shift. They observed a small quadratic shift of up to about 0.4 meV for both the exciton and trion in monolayer MoS$_2$ encapsulated in hexagonal boron nitride
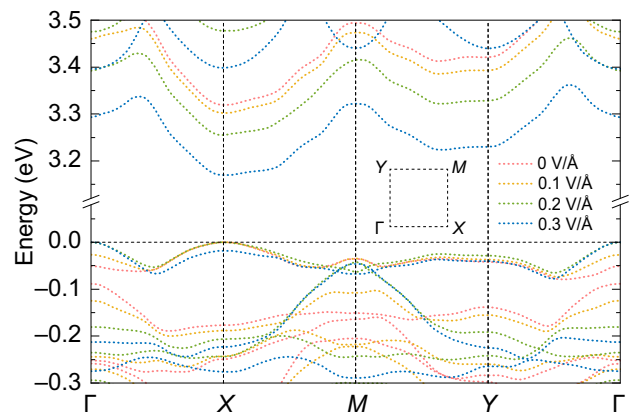

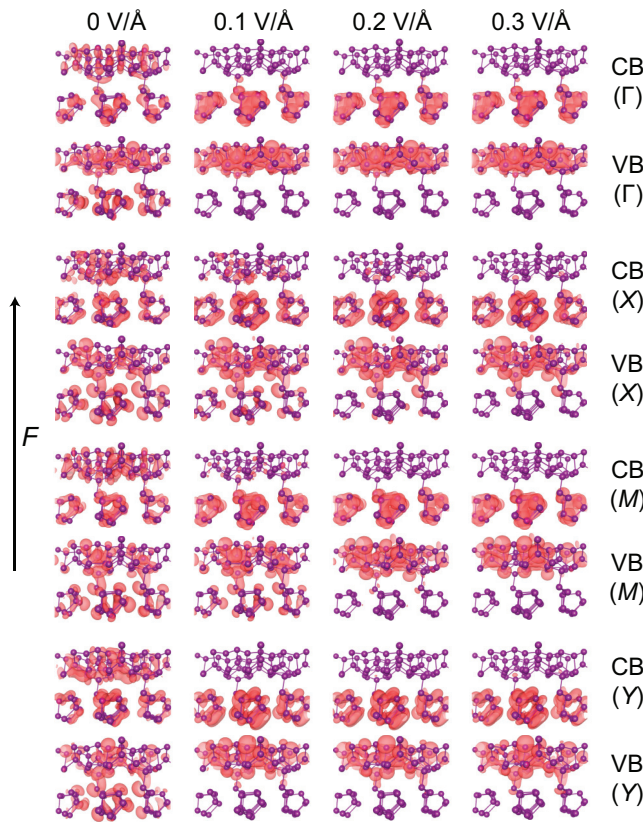FIG. 5. Quasiparticle band structure of Hittorf's phosphorene under an applied electric field.

FIG. 6. Effect of an electric field on the distribution of electrons and holes among the monolayer structure of Hittorf's phosphorene. Electronic states at four high-symmetry k points are presented.

FIG. 8. Optical absorption of Hittorf's phosphorene under an applied electric field. (a) Polarization along the x axis. (b) Polarization along the y axis. (c) The averaged value.

surface potential fluctuations. With the above consideration, it could be concluded the QCSE is much larger in Hittorf's phosphorene than that in TMDs.

B. Evolution of excitons in Hittorf's phosphorene under an out-of-plane electric field

The detailed exciton spectrum of Hittorf's phosphorene and its evolution under an electric field are presented in Fig. 13, where the red and blue lines indicate the bright excitons excited by light polarized along the x and y directions, respectively. The exciton energies are consistent with optical absorption spectrum demonstrated before and the absorption edge is consistent with the position of the
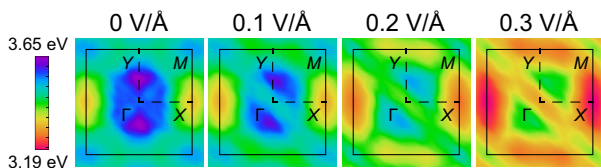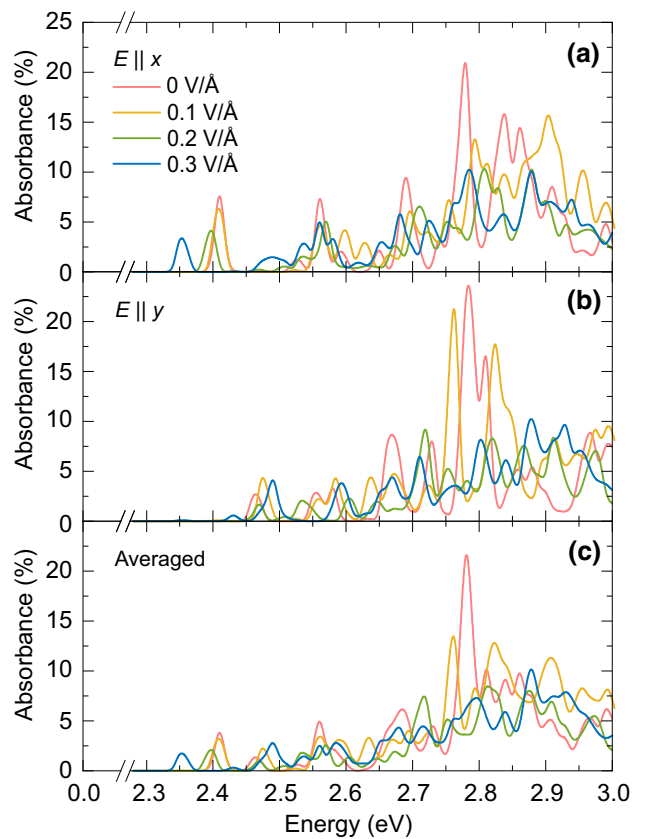
first exciton. The excitation anisotropy, i.e., the difference between the first two exciton states, is 55 meV at zero bias, and is enhanced to 77 meV under an electric field of 0.3 V/Å.

In Fig. 14, we provide detailed information for the first exciton state and investigate its electric field dependence.

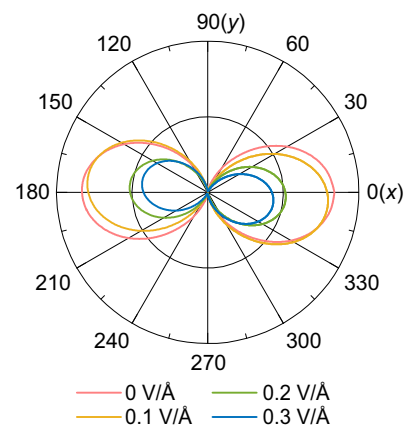FIG. 7. Evolution of the lowest direct transitions of Hittorf's phosphorene under an electric field.

FIG. 9. Optical anisotropy from the first excitonic state under an applied electric field.
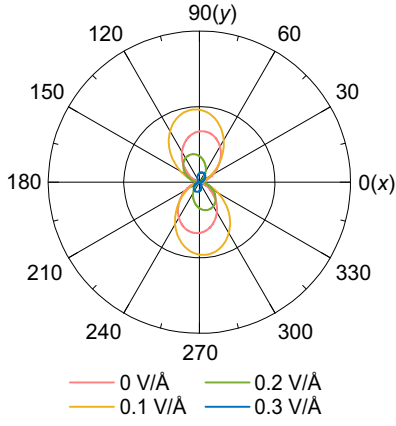
FIG. 10. Optical anisotropy from the second excitonic state under an applied electric field.

Because of the effective dissociation of the electron and the hole by an external electric field, the overlap between their wave functions gets weak. As shown in Fig. 14(a), μ_S^2 exhibits a significant decrease, in particular at high fields. The exciton binding energy shown in Fig. 14(b) decreases from 91 meV at zero bias to 83 meV at 0.3 V/Å. The effective mass M_S presented in Fig. 14(c), on the other hand, shows an increase. The increase is less than 10% up to a field of 0.3 V/Å. In general, the larger the band gap, the stronger the exciton binding energy and effective mass. Such evolutions indicate that the electric field has a subtle and complicated influence on the behaviors of electrons and holes. As shown in Fig. 14(d), the exciton lifetime $\langle \tau_S \rangle$ at room temperature increases significantly with the applied electric field, showing the possible tunability and optimization of the performance for 2D LED devices.

To understand the above dependencies further, we resort back to dielectric screening of the system as well as its electric field dependence. It should be pointed out that what we have simulated is a suspended monolayer, i.e., 2D Hittorf's phosphorene in vacuum. The strength of the
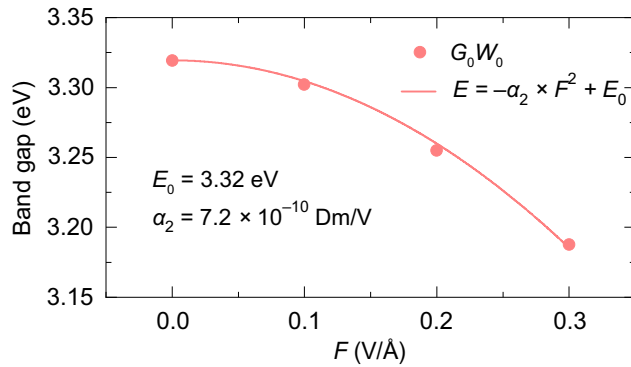

FIG. 11. Evolution of the quasiparticle band gap (at the X point) of Hittorf's phosphorene under an electric field.
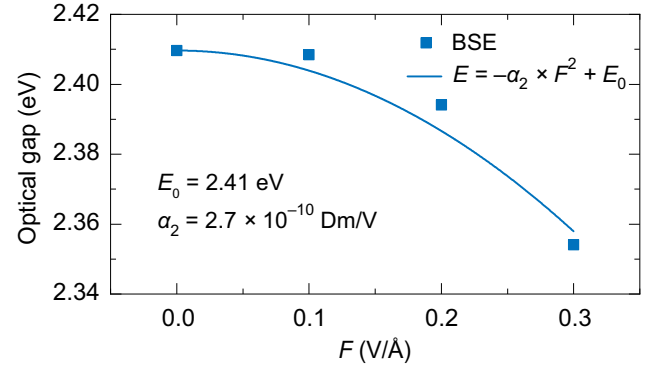

FIG. 12. Evolution of the optical gap of Hittorf's phosphorene under an electric field.

Coulomb interaction in these materials originates from weak dielectric screening in the 2D limit [8,11,16,18,43]. For distances exceeding a few nanometres, the screening is determined by the immediate surroundings of the material, which can be vacuum or air in the ideal case of suspended samples. The static screened Coulomb interaction is constructed as [74]

$$W_{\mathbf{GG'}}(\mathbf{q};0) = \epsilon_{\mathbf{GG'}}^{-1}(\mathbf{q};0)v(\mathbf{q}+\mathbf{G'}). \quad (3)$$

The effective static 2D dielectric function $\epsilon_{2D}(q)$ could be obtained as [17]

$$\epsilon_{2D}^{-1}(q) = \frac{q}{2\pi e^2 L_z} \sum_{\mathbf{G}_z \mathbf{G}_z'} W_{\mathbf{G}_z \mathbf{G}_z'}(q), \quad (4)$$

where the complicated details of the screening in the out-of-plane direction z have been integrated out. The dielectric screening in such a system obeys a particular wavelength dependence. As described in Fig. 15(a) for Hittorf's phosphorene, for the long-distance limit, the electrons interact like that in a vacuum with $\epsilon = 1$, while in the intermediate distance, the electron-electron interaction has effective dielectric screening by the 2D materials with $\epsilon \geq 1$. Interestingly, the dielectric function almost remains the same when the electric field is applied. In 2D materials,

TABLE II. The calculated quasiparticle band-gap reduction with an electric field at different high-symmetry k points (Γ, X, M, and Y), optical gap reduction, and corresponding polarizability α_2 of Hittorf's phosphorene. Results within PBE are listed in parentheses.

ΔE (meV)	0.1 V/Å	0.2 V/Å	0.3 V/Å	α_2 (10^{-10} Dm/V)
Γ	66 (78)	161 (175)	260 (276)	15.0 (16.0)
X	17 (22)	64 (78)	132 (152)	7.2 (8.4)
M	21 (32)	50 (106)	140 (208)	11.0 (12.0)
Y	33 (41)	106 (121)	193 (211)	7.3 (11.0)
Optical	1	16	56	2.7

TABLE III. Experimental approaches of QCSE in TMDs using various fabrication methods, device structures, maximal applied fields F, maximal optical gap reductions ΔE, and polarizabilities α_2.

	Fabrication	Device structure	Maximal F (V/Å)	Maximal ΔE (meV)	α_2 (Dm/V)
MoS_2 [50]	Mechanically exfoliated	Encapsulated between SiO_2 and Al_2O_3	0.03	6.8	4.5×10^{-9}
MoS_2 [55]	Mechanically exfoliated	Encapsulated in h-BN	0.017	0.44	7.8×10^{-10}
WSe_2 [60]	Mechanically exfoliated	Encapsulated between h-BN and few-layer graphene	0.16	0.4	$\sim 10^{-11}$
WS_2 [61]	CVD growth	Heterostructure with graphite	0.02	0.4	4.8×10^{-10}
WS_2 [64]	Mechanically exfoliated	Encapsulated between h-BN and few-layer graphene	0.06	11.7	1.11×10^{-9}

$\epsilon_{2D}(q) = 1 + 2\pi q \alpha_{2D}$, where α_{2D} is the 2D polarizability and can be obtained by fitting the dielectric function at the long-wavelength limit $q \rightarrow 0$ [9]. In Fig. 15(b), we find a very slight increase in the polarizability when the electric field is applied. These results indicate that the dielectric screening environment in monolayer Hittorf's phosphorene is robust against the applied electric field. This is reasonable, because although the band gap changes around 4% for the highest field of 0.3 V/Å, the product of the wave function in the equation for polarizability [see Eq. (A1)] could also be reduced for the separation of electron and hole wave functions under an applied field. Such a static dielectric function change is very small. The revealed, almost unchangeable, static dielectric screening with external electric field, as we know, can be expected in other 2D materials, where the band-gap reduction under an out-of-plane electric field can be neglectful. The effect of the electric field on the excitonic properties, on the other hand, should be tightly related to the unique sublayer structure in

Hittorf's phosphorene monolayer, where the electron-hole pairs near band edges are effectively separated by an external out-of-plane electric field. By now, we have arrived at a clear picture of the evolution of the quasiparticle band structure, optical properties, and exciton properties under an applied out-of-plane electric field. The competition between the reduction in the band gap and the suppression of the exciton binding energy is then evident.

It is interesting to present the wave functions of the exciton state. The first exciton is plotted in Fig. 16. The green dot indicates the position of the hole, where we distinguish and compare three cases with the hole located at two neighboring sublayers and intersublayer space, respectively. The overall character of these excitons is that the spatial distribution of their wave function is along tubes, which is due to the geometry of the crossing-tube structure of Hittorf's phosphorene. In the absence of an external electric field, the exciton wave function reaches maximum spatial distribution when the hole is fixed at the center of a P—P bond between two sublayers. After applying an electric field, the electrons are gradually driven downwards. From the top view, the planar distribution gets wider and asymmetry between the two sublayers is more obvious. These variations can explain the slight enhancement of the optical anisotropy in the absorption spectra. When we increase the electric field further, holes get recovered at the lower part of each sublayer. The envelope functions in reciprocal space of the first exciton state are presented in Fig. 17. The first exciton state arises mainly from the electron-hole excitations at the X point, consistent with the valley profile revealed above.

It is noted that the electric field dependence of the energy of the second exciton shows nonmonotonic behavior. As shown in Fig. 13, the energy first shows an increase to higher energy under an electric field of 0.1 V/Å. The decrease of the exciton state to lower energies is only observed when the electric field is larger than 0.2 V/Å. The wave functions of the second exciton state are also plotted in Fig. 18. Compared with the first exciton state, these exciton wave functions show similar distributions,
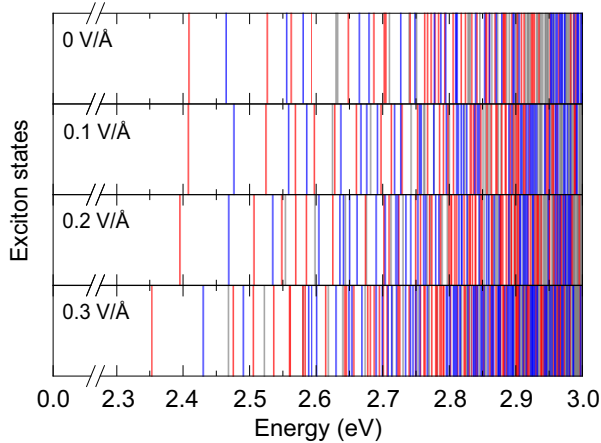

FIG. 13. Exciton spectrum of Hittorf's phosphorene under applied electric fields. Red and blue lines are for the bright exciton states, and gray lines are for the dark exciton states.
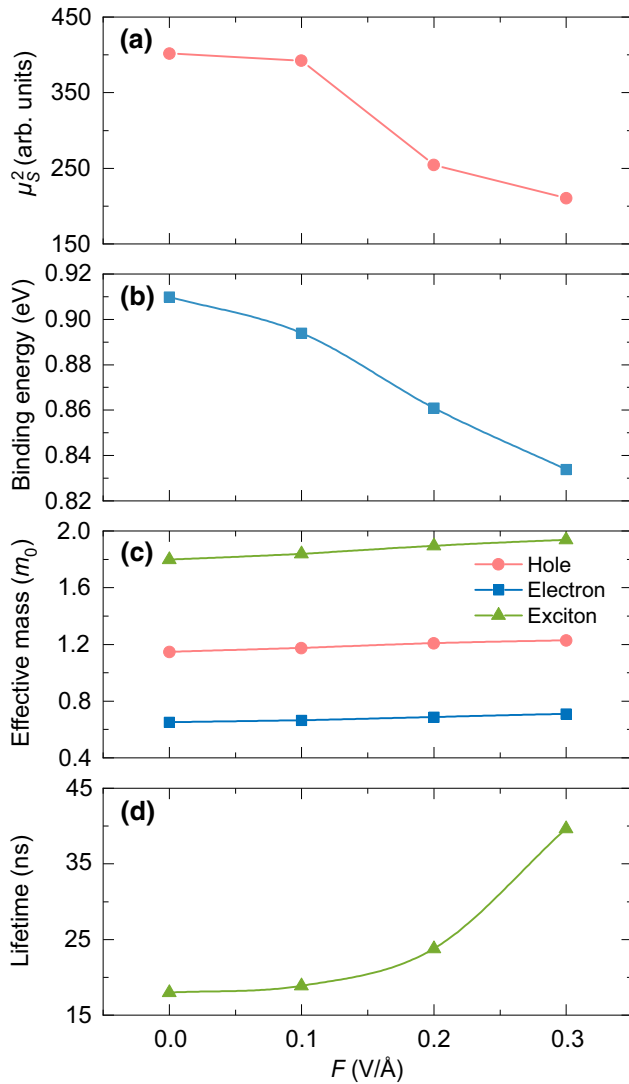
FIG. 14. Evolution of excitonic properties under an electric field in Hittorf's phosphorene. (a) Oscillator strength. (b) Binding energy. (c) Effective mass. (d) Lifetime.

FIG. 15. Dielectric screening in Hittorf's phosphorene under an applied electric field. (a) The q dependence of the 2D static dielectric constant and (b) the 2D polarizability.

C. Applications of QCSE in Hittorf's phosphorene in optoelectronics

It is noted that, for QCSE, the most promising application lies in its ability to perform optical

FIG. 16. Evolution of the real-space modulus squared of the wave function of the first exciton under an electric field. The green dot indicates the hole position. From top to bottom, we show three cases with the hole placed at the top layer (top panels), interlayer (middle panels), and bottom layer (bottom panels).

both of which are distributed along the tube directions. It is also noted that the wave functions of the second exciton are more localized in the lower sublayer and exhibit strong anisotropic planar distribution after applying the electric field. This suggests a more dramatic weakening of electron-hole interactions and, therefore, a substantial lowering of exciton binding energy as well as optical absorption amplitude. In reciprocal space, as shown in Fig. 19, the second exciton firstly arises from the transition mainly located at the X point for fields smaller than 0.2 V/Å. When the field reaches as high as 0.3 V/Å, the center changes to the Y point. The detailed components are shown in Fig. 20, where the composition of the second exciton state is more complicated than the first one.
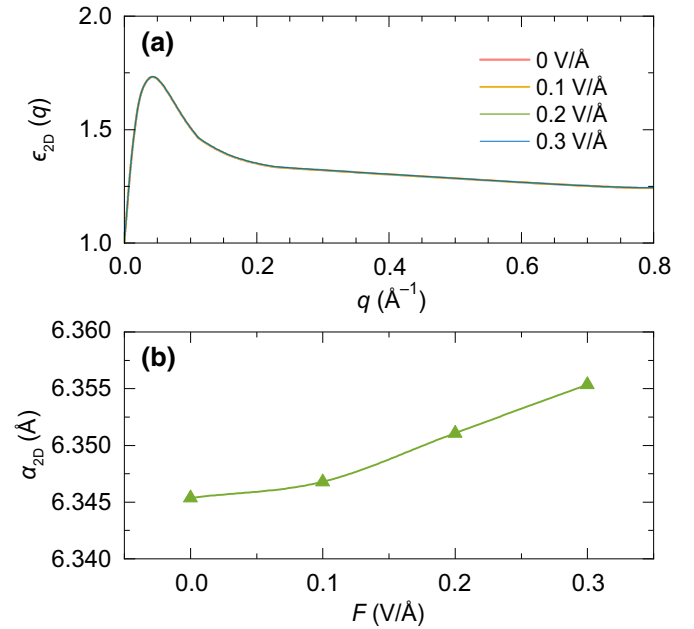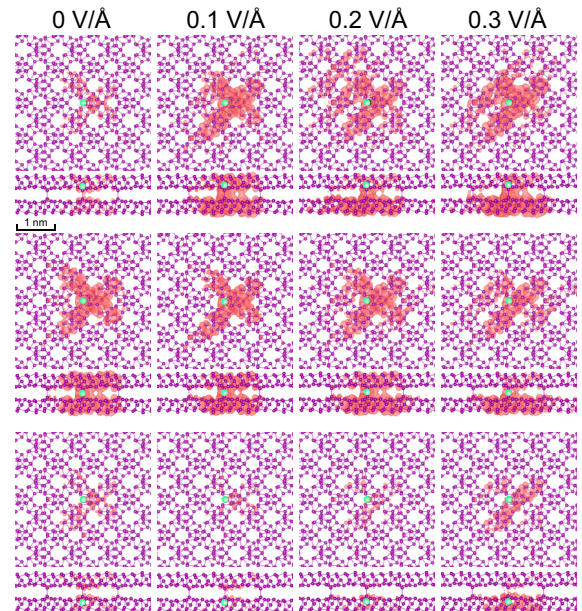
FIG. 17. The *k*-space modulus squared of the wave function of the first exciton under an applied electric field.

modulation [83], which is particularly desirable for data communication link applications. Since the first demonstration in GaAs/Al$_x$Ga$_{1-x}$As quantum wells [41,42], QCSE started to generate technological interest after its demonstration in Ge/SiGe [84]. The epitaxial growth of Ge on top of a silicon substrate is a decisive advantage as it allows Ge/SiGe QCSE to be integrated with complementary metal-oxide-semiconductor (CMOS) technology and silicon photonics systems. Because of the narrow band gap in Ge, QCSE in Ge/SiGe quantum wells can therefore be used to modulate light at 1.55 μm, which is crucial for silicon photonics applications as 1.55 μm is the optical fiber's transparency window and the most extensively employed wavelength for telecommunications. The advantage of 2D materials is the easy compatibility with different photonic structures [85]. In particular, 2D materials offer potential for large-scale and low-cost integration into the current dominant optical fiber network and silicon

FIG. 19. The *k*-space plots of the modulus squared of the wave function for the second exciton under applied electric fields. From the top to bottom are the overall and band-to-band decomposed plots.

CMOS technology [85]. In fact, the gate-tunable electroabsorption effect in graphene has been utilized for electro-optic modulators [86,87]. The applications of QCSE in 2D materials have not yet been experimentally addressed [85], which is due to the small magnitude of absolute absorption of the monolayer and the small QCSE itself in the monolayers as mentioned above. Since the QCSE in Hittorf's phosphorene is almost 30 times larger than TMDs,

FIG. 18. Evolution of the real-space modulus squared of the wave function of the second exciton under an electric field. The green dot indicates the hole position. From top to bottom, we show three cases with the hole placed at the top layer (top panels), interlayer (middle panels), and bottom layer (bottom panels).
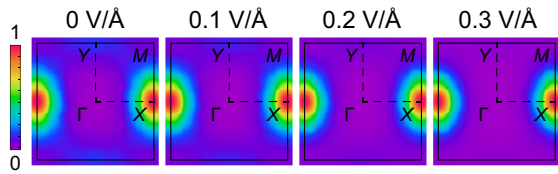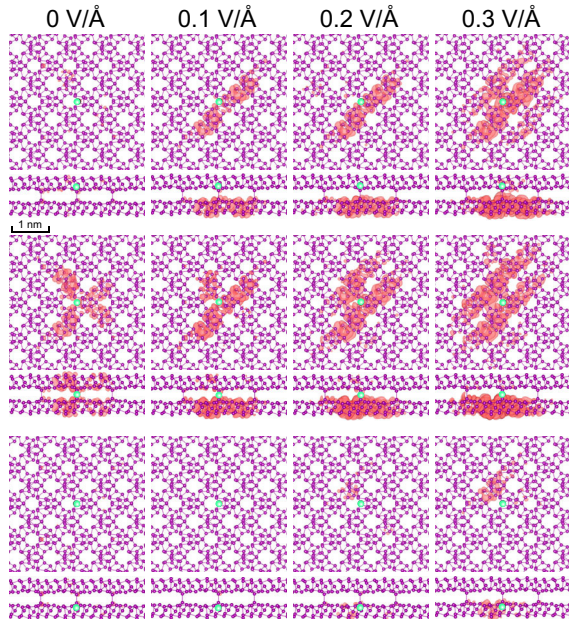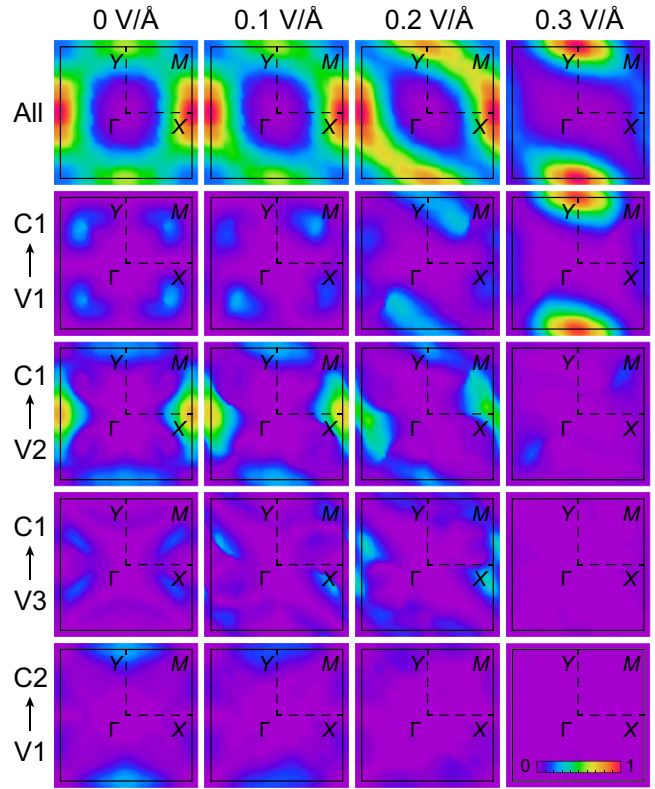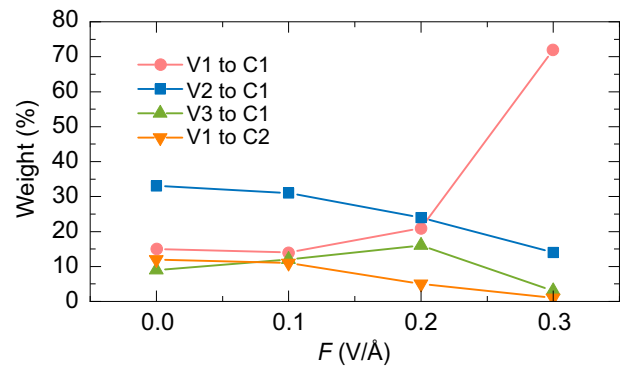

FIG. 20. Evolution of the relative weight for the various band-to-band transitions in composing the second exciton state under an electric field.

it is promising for the application of Hittorf's phosphorene as electro-optical modulators. The modulation depth is typically described by the ratio between the maximum and the minimum transmittances (T_{max}/T_{min}) and here we calculate the modulation depth in decibel units by $10 \times \log(T_{max}/T_{min})$ (T equals 1 minus the absorbance $\mathcal{A}$, as shown in Fig. 8) [85]. In Hittorf's phosphorene, for light at 2.8 eV (polarized along the y direction), the optical signal modulation could reach as high as 1.4 dB at an electric field of 0.1 V/Å (as derived from the data shown in Fig. 8). For light polarized along the x direction, the modulation also reaches 1.2 dB at around 2.8 eV. For unpolarized light, the modulation is still as large as 1.1 dB. These values are much larger than 0.1 dB that has been revealed in monolayer graphene [85]. Therefore, QCSE-based optical modulation in Hittorf's phosphorene is hopeful for relevant applications of electro-optical modulation. On the other hand, QCSE is essential for the functionality in light-emitting systems. For the single light emitter in layered hexagonal boron nitride, a Stark tuning of 7.7 meV (5.5 nm) is reported at an electric field of 0.02 V/Å, exceeding the resonance linewidth of typical nanodielectric and nanoplasmonic resonators [88]. The Stark shift in Hittorf's phosphorene could also be large, with a value of up to 56 meV (12.2 nm) at 0.3 V/Å. Such a giant Stark effect in Hittorf's phosphorene provides obvious advantages in the realization of a sensitive sensor of the electric field [89].

IV. SUMMARY

To summarize, based on DFT with the G_0W_0-BSE framework, we have revealed large QCSEs in Hittorf's phosphorene. Quantum-confined geometry with enhanced electron-electron interaction and a relatively large thickness of this monolayer structure are essential in the effective reduction of the quasiparticle band gap under out-of-plane electric fields. The unique bisublayer crystal structure, on the other hand, gives rise to spatial separation of photoexcited electron-hole pairs and the obvious reduction of the optical absorption edge and exciton binding energy under electric fields. The static macroscopic dielectric screening in fact changes little with applied electric field, showing the subtle and complicated relationship between the quasiparticle band gap, band dispersion (effective mass), and excitonic properties in 2D materials. The crystal-structure-favored spatial separation and localization of electron and hole wave functions near the band edges have been shown to be key to understanding these behaviors, while the direct band gap and short lifetime of the exciton in pristine Hittorf's phosphorene has been shown to be beneficial for efficient green light emitting [34]. The robust electric field tunable optical absorption and excitonic properties revealed in this study have demonstrated wide applications of Hittorf's phosphorene in 2D optoelectronic devices, e.g., electro-optical modulators (amplitude and phase) and light-emitting systems (amplitude and wavelength).

APPENDIX A: G_0W_0-BSE APPROACH

Generally, the quasiparticle self-energies are obtained by solving the Dyson equation [74]. The self-energy operator Σ is invoked for the quasiparticle behavior with quasiparticle energies $E_{n\mathbf{k}}^{QP}$ and wave functions $\psi_{n\mathbf{k}}^{QP}$. Here, we use the many-body perturbation method with the one-shot G_0W_0 framework. The mean-field wave functions within DFT-PBE are used as quasiparticle wave functions and the quasiparticle energy is approached by starting from the DFT-PBE eigenvalue.

We first compute static polarizability based on the random-phase approximation (RPA) [74]:

$$\chi_{\mathbf{GG'}}(\mathbf{q};0) = \sum_{n,n',\mathbf{k}} \langle n, \mathbf{k}|e^{-i(\mathbf{q}+\mathbf{G})\cdot\mathbf{r}}|n', \mathbf{k}+\mathbf{q}\rangle$$
$$\times \langle n', \mathbf{k}+\mathbf{q}|e^{i(\mathbf{q}+\mathbf{G'})\cdot\mathbf{r'}}|n, \mathbf{k}\rangle \frac{1}{E_{n'\mathbf{k}+\mathbf{q}} - E_{n\mathbf{k}}}. \tag{A1}$$

Here n, n' are occupied and unoccupied band indices, $\mathbf{k}$ is the wave vector, $\mathbf{q}$ is a vector in the first Brillouin zone, $\mathbf{G}$ is a reciprocal-lattice vector, and $|n, \mathbf{k}\rangle$ and $E_{n\mathbf{k}}$ are the mean-field electronic eigenvectors and eigenvalues, respectively.

Then the dielectric matrix is constructed as [74]

$$\epsilon_{\mathbf{GG'}}(\mathbf{q};0) = \delta_{\mathbf{GG'}} - v(\mathbf{q}+\mathbf{G})\chi_{\mathbf{GG'}}(\mathbf{q};0) \tag{A2}$$

with the slab-truncated Coulomb interaction included [77],

$$v_t^{slab}(\mathbf{q}) = \frac{4\pi}{q^2} \times [1 - e^{-q_{xy} \times z_c}\cos(q_z \times z_c)], \tag{A3}$$

where z_c is the truncation distance in the perpendicular direction. Such a treatment could guarantee the convergence of dielectric screening ("head" in $\epsilon_{\mathbf{GG'}}$) to approach unity in the long-wavelength limit [11,12,14–20,22,26–30, 34–37].

Within the generalized plasmon pole (GPP) model, the imaginary and real parts of the inverse dielectric matrix with finite frequencies are given by [74]

$$\mathrm{Im}\epsilon_{\mathbf{G}\mathbf{G}'}^{-1}(\mathbf{q},\omega) = -\frac{\pi}{2}\frac{\Omega_{\mathbf{G}\mathbf{G}'}(\mathbf{q})}{\tilde{\omega}_{\mathbf{G}\mathbf{G}'}(\mathbf{q})}\{\delta[\omega - \tilde{\omega}_{\mathbf{G}\mathbf{G}'}(\mathbf{q})]$$
$$- \delta[\omega + \tilde{\omega}_{\mathbf{G}\mathbf{G}'}(\mathbf{q})]\} \qquad \text{(A4)}$$

and

$$\mathrm{Re}\epsilon_{\mathbf{G}\mathbf{G}'}^{-1}(\mathbf{q},\omega) = 1 + \frac{\Omega_{\mathbf{G}\mathbf{G}'}^2(\mathbf{q})}{\omega^2 - \tilde{\omega}_{\mathbf{G}\mathbf{G}'}^2(\mathbf{q})}, \qquad \text{(A5)}$$

where $\Omega_{\mathbf{G}\mathbf{G}'}(\mathbf{q})$ and $\tilde{\omega}_{\mathbf{G}\mathbf{G}'}(\mathbf{q})$ are the effective bare plasma frequency and the GPP mode frequency defined as [74]

$$\Omega_{\mathbf{G}\mathbf{G}'}^2(\mathbf{q}) = \omega_p^2 \frac{(\mathbf{q}+\mathbf{G})\cdot(\mathbf{q}+\mathbf{G}')}{|\mathbf{q}+\mathbf{G}|^2}\frac{\rho(\mathbf{G}-\mathbf{G}')}{\rho(\mathbf{0})}, \qquad \text{(A6)}$$

$$\tilde{\omega}_{\mathbf{G}\mathbf{G}'}^2(\mathbf{q}) = \frac{\Omega_{\mathbf{G}\mathbf{G}'}^2(\mathbf{q})}{\delta_{\mathbf{G}\mathbf{G}'} - \epsilon_{\mathbf{G}\mathbf{G}'}^{-1}(\mathbf{q},\omega=0)}. \qquad \text{(A7)}$$

Here ρ is the electron charge density in reciprocal space and $\omega_p^2 = 4\pi\rho(\mathbf{0})e^2/m$ is the classical plasma frequency.

Using the form of the above frequency-dependent dielectric function, the self-energy operator Σ is solved in two parts, $\Sigma = \Sigma_{\mathrm{SEX}} + \Sigma_{\mathrm{COH}}$, where Σ_{SEX} is the screened exchange operator and Σ_{COH} is the Coulomb-hole operator, as [74]

$$\langle n,\mathbf{k}|\Sigma_{\mathrm{SEX}}(E)|n',\mathbf{k}\rangle$$
$$= -\sum_{n_1}^{\mathrm{occ}}\sum_{\mathbf{q},\mathbf{G},\mathbf{G}'}\langle n,\mathbf{k}|e^{i(\mathbf{q}+\mathbf{G})\cdot\mathbf{r}}|n_1,\mathbf{k}-\mathbf{q}\rangle\langle n_1,\mathbf{k}-\mathbf{q}$$
$$|e^{-i(\mathbf{q}+\mathbf{G}')\cdot\mathbf{r}'}|n',\mathbf{k}\rangle$$
$$\times\left(1 + \frac{\Omega_{\mathbf{G}\mathbf{G}'}^2(\mathbf{q})}{(E - E_{n_1\mathbf{k}-\mathbf{q}})^2 - \tilde{\omega}_{\mathbf{G}\mathbf{G}'}^2(\mathbf{q})}\right)v(\mathbf{q}+\mathbf{G}') \quad \text{(A8)}$$

and

$$\langle n,\mathbf{k}|\Sigma_{\mathrm{COH}}(E)|n',\mathbf{k}\rangle$$
$$= \sum_{n_1}\sum_{\mathbf{q},\mathbf{G},\mathbf{G}'}\langle n,\mathbf{k}|e^{i(\mathbf{q}+\mathbf{G})\cdot\mathbf{r}}|n_1,\mathbf{k}-\mathbf{q}\rangle\langle n_1,\mathbf{k}-\mathbf{q}$$
$$|e^{-i(\mathbf{q}+\mathbf{G}')\cdot\mathbf{r}'}|n',\mathbf{k}\rangle$$
$$\times\frac{1}{2}\frac{\Omega_{\mathbf{G}\mathbf{G}'}^2(\mathbf{q})}{\tilde{\omega}_{\mathbf{G}\mathbf{G}'}(\mathbf{q})[E - E_{n_1\mathbf{k}-\mathbf{q}} - \tilde{\omega}_{\mathbf{G}\mathbf{G}'}(\mathbf{q})]}v(\mathbf{q}+\mathbf{G}'). \quad \text{(A9)}$$

With the above obtained quasiparticle energies and static dielectric screening from RPA, the electron-hole excitations are then calculated by solving the BSE for each

exciton state S [75]:

$$(E_{c\mathbf{k}}^{\mathrm{QP}} - E_{v\mathbf{k}}^{\mathrm{QP}})A_{vc\mathbf{k}}^S + \sum_{v'c'\mathbf{k}'}\langle vc\mathbf{k}|K^{\mathrm{eh}}|v'c'\mathbf{k}'\rangle A_{v'c'\mathbf{k}'}^S = \Omega^S A_{vc\mathbf{k}}^S. \qquad \text{(A10)}$$

Here $A_{vc\mathbf{k}}^S$ is the exciton wave function, Ω^S is the excitation energy, and K^{eh} is the electron-hole interaction kernel.

The kernel contains two terms, a screened direct interaction and a bare exchange interaction, $K^{\mathrm{eh}} = K^{\mathrm{d}} + K^{\mathrm{x}}$, defined as [75]

$$\langle vc\mathbf{k}|K^{\mathrm{d}}|v'c'\mathbf{k}'\rangle = \sum_{\mathbf{G}\mathbf{G}'}\langle c,\mathbf{k}+\mathbf{q}|e^{-i(\mathbf{q}+\mathbf{G})\cdot\mathbf{r}}|c',\mathbf{k}\rangle$$
$$W_{\mathbf{G}\mathbf{G}'}(\mathbf{q};0)\langle v',\mathbf{k}|e^{i(\mathbf{q}+\mathbf{G}')\cdot\mathbf{r}}|v,\mathbf{k}+\mathbf{q}\rangle \qquad \text{(A11)}$$

and

$$\langle vc\mathbf{k}|K^{\mathrm{x}}|v'c'\mathbf{k}'\rangle = \sum_{\mathbf{G}\mathbf{G}'}\langle c,\mathbf{k}+\mathbf{q}|e^{-i(\mathbf{q}+\mathbf{G})\cdot\mathbf{r}}|v,\mathbf{k}\rangle$$
$$\delta_{\mathbf{G}\mathbf{G}'}v(\mathbf{q}+\mathbf{G})\langle v',\mathbf{k}|e^{i(\mathbf{q}+\mathbf{G}')\cdot\mathbf{r}}|c',\mathbf{k}+\mathbf{q}\rangle. \qquad \text{(A12)}$$

Finally, we obtain the imaginary parts of the frequency-dependent complex dielectric function $\epsilon_2(\omega)$ as [75]

$$\epsilon_2(\omega) = \frac{16\pi^2 e^2}{\omega^2}\sum_S |\mathbf{e}\cdot\langle 0|\mathbf{v}|S\rangle|^2\delta(\omega - \Omega^S), \qquad \text{(A13)}$$

where $\mathbf{v}$ is the velocity operator and $\mathbf{e}$ is the polarization of the incoming light. Here, we use absorbance $\mathcal{A}$ of 2D materials to measure its optical properties, which is expressed as [35]

$$\mathcal{A}(\omega) = 1 - e^{-\alpha(\omega)d} = 1 - e^{-\omega\epsilon_2 d/\hbar c}, \qquad \text{(A14)}$$

where α is the absorption coefficient, d is the thickness of the simulation cell along the direction perpendicular to the layer, ϵ_2 is the imaginary part of the dielectric function, and ω is the photon energy.

To access the excitonic properties of Hittorf's phosphorene further, we calculate the lifetime of the first bright exciton and its evolution under an out-of-plane electric field. Using Fermi's golden rule, the radiative lifetime $\tau_S(0)$ at 0 K of an exciton in state S is derived according to [79,80]

$$\tau_S(0) = \frac{\hbar^2 c}{4\pi e^2 E_S(0)}\frac{A_{\mathrm{u.c.}}}{\mu_S^2}, \qquad \text{(A15)}$$

where c is the speed of light, $A_{\mathrm{u.c.}}$ is the area of the unit cell, $E_S(0)$ is the energy of the exciton in state S, and $\mu_S^2 =$

$(\hbar^2/m^2 E_S(0)^2)(|\langle G|p_\parallel|\Psi_S\rangle|^2/N_k)$ is the square modulus of the BSE exciton transition dipole divided by the number of unit cells in this 2D system. We obtain the exciton radiative lifetime $\langle \tau_S \rangle$ at temperature T as

$$\langle \tau_S \rangle = \tau_S(0) \frac{3}{4} \left(\frac{E_S(0)^2}{2 M_S c^2} \right)^{-1} k_B T, \qquad (A16)$$

where k_B is Boltzmann's constant and $M_S = m_e^* + m_h^*$ is the exciton mass.

FIG. 21. Evolution of the band structure of Hittorf's phosphorene (within PBE) under an electric field.

APPENDIX B: CRYSTAL STRUCTURE OF HITTORF'S PHOSPHORENE

In Table IV, we show the optimized crystal structure of Hittorf's phosphorene [34]. The original atomic position is from the bulk counterpart [31].

APPENDIX C: ELECTRONIC BAND STRUCTURE OF HITTORF'S PHOSPHORENE WITHIN THE CALCULATIONS OF PBE

In Fig. 21, we show the PBE band structure of Hittorf's phosphorene under different electric fields.
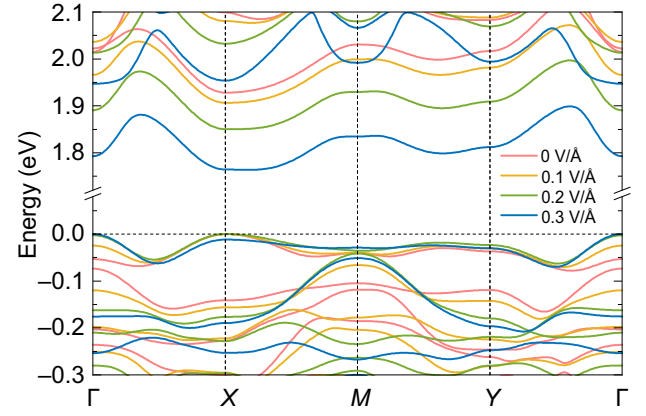
APPENDIX D: OPTICAL ABSORBANCE OBTAINED WITHOUT CONSIDERATION OF THE ELECTRON-HOLE INTERACTION

In Fig. 22, we provide the optical absorption spectrum without the inclusion of the electron-hole interaction. Clearly, due to the absence of the excitonic effect, the optical absorption spectrum is continuous and shows a monotonic decrease to lower energies due to the reduction in the band gap under an applied field. In the meantime, the absorption strength changes for the modification of electron-hole wave functions near band edges for the optical transitions.

TABLE IV. Optimized atomic positions (fractional coordinates in terms of the lattice constants) for 2D Hittorf's phosphorene with the lattice constants $a = 9.24$ (Å), $b = 9.26$ (Å), and $c = 30.16$ (Å) [34].

| Atom	x	y	z	Atom	x	y	z
P1	0.672 558	0.975 614	0.535 874	P22	0.852 486	0.898 953	0.631 000
P2	0.788 657	0.341 854	0.554 517	P23	0.078 462	0.110 784	0.345 280
P3	0.955 498	0.743 475	0.399 042	P24	0.078 462	0.889 215	0.654 719
P4	0.955 498	0.256 524	0.600 957	P25	0.131 208	0.340 541	0.356 463
P5	0.207 324	0.989 830	0.398 552	P26	0.131 208	0.659 458	0.643 536
P6	0.207 324	0.010 169	0.601 447	P27	0.358 966	0.339 682	0.333 279
P7	0.042 184	0.909 282	0.445 232	P28	0.358 966	0.660 317	0.666 720
P8	0.042 184	0.090 717	0.554 767	P29	0.358 960	0.567 229	0.356 215
P9	0.309 528	0.163 919	0.437 620	P30	0.358 960	0.432 770	0.643 784
P10	0.309 528	0.836 080	0.562 379	P31	0.589 423	0.619 228	0.344 934
P11	0.480 191	0.218 842	0.388 956	P32	0.589 423	0.380 771	0.655 065
P12	0.480 191	0.781 157	0.611 043	P33	0.603 248	0.807 543	0.440 816
P13	0.535 737	0.389 760	0.437 305	P34	0.603 248	0.192 456	0.559 183
P14	0.535 737	0.610 239	0.562 694	P35	0.891 170	0.094 300	0.441 859
P15	0.710 582	0.492 219	0.398 650	P36	0.891 170	0.905 699	0.558 140
P16	0.710 581	0.507 780	0.601 349	P37	0.166 072	0.357 352	0.429 711
P17	0.598 173	0.845 290	0.368 081	P38	0.166 072	0.642 646	0.570 288
P18	0.598 173	0.154 710	0.631 918	P39	0.341 629	0.532 584	0.429 541
P19	0.828 000	0.872 082	0.347 673	P40	0.341 629	0.467 415	0.570 458
P20	0.828 000	0.127 917	0.652 326	P41	0.672 558	0.024 385	0.464 125
P21	0.852 486	0.101 046	0.368 999	P42	0.788 657	0.658 145	0.445 482
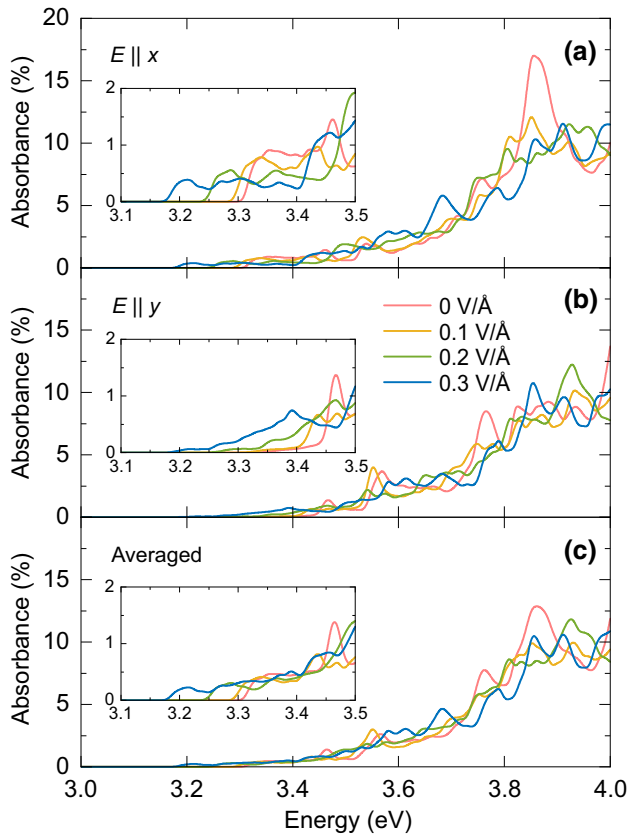
FIG. 22. Optical absorption of Hittorf's phosphorene under an applied electric field. Here, the calculations are obtained without consideration of the electron-hole interaction. (a) Polarization along the x axis. (b) Polarization along the y axis. (c) The averaged value.

APPENDIX E: ELECTRONIC BAND STRUCTURE AND EVOLUTION OF THE BAND GAP OF HITTORF'S PHOSPHORENE WITHIN THE CALCULATIONS OF PBE

The evolution of the band gap at a high-symmetry k point (X point) under an electric field is shown in Fig. 23, with the fitting equation illustrated.
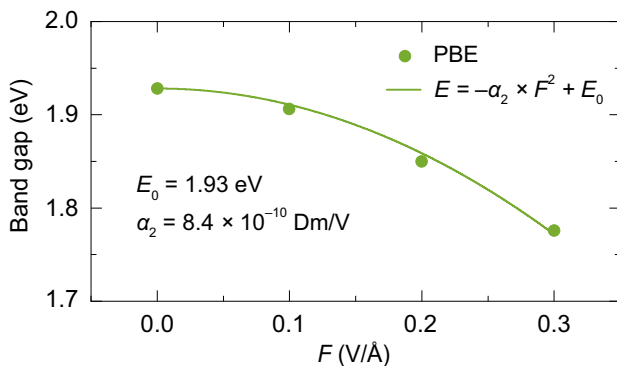

FIG. 23. Evolution of the band gap (within PBE) of Hittorf's phosphorene (at the X point) under an electric field.

[1] A. H. Castro Neto, F. Guinea, N. M. R. Peres, K. S. Novoselov, and A. K. Geim, The electronic properties of graphene, Rev. Mod. Phys. **81,** 109 (2009).

[2] D. N. Basov, M. M. Fogler, A. Lanzara, F. Wang, and Y. Zhang, Colloquium: Graphene spectroscopy, Rev. Mod. Phys. **86,** 959 (2014).

[3] G. Wang, A. Chernikov, M. M. Glazov, T. F. Heinz, X. Marie, T. Amand, and B. Urbaszek, Excitons in atomically thin transition metal dichalcogenides, Rev. Mod. Phys. **90,** 021001 (2018).

[4] F. Xia, H. Wang, J. C. M. Hwang, A. H. Castro Neto, and L. Yang, Black phosphorus and its isoelectronic materials, Nat. Rev. Phys. **1,** 306 (2019).

[5] A. Rodin, M. Trushin, A. Carvalho, and A. H. Castro Neto, Collective excitations in 2D materials, Nat. Rev. Phys. **2,** 524 (2020).

[6] S. Shree, I. Paradisanos, X. Marie, C. Robert, and B. Urbaszek, Guide to optical spectroscopy of layered semiconductors, Nat. Rev. Phys. **3,** 39 (2021).

[7] L. Yang, J. Deslippe, C. H. Park, M. L. Cohen, and S. G. Louie, Excitonic Effects on the Optical Response of Graphene and Bilayer Graphene, Phys. Rev. Lett. **103,** 186802 (2009).

[8] P. Cudazzo, C. Attaccalite, I. V. Tokatly, and A. Rubio, Strong Charge-Transfer Excitonic Effects and the Bose-Einstein Exciton Condensate in Graphane, Phys. Rev. Lett. **104,** 226804 (2010).

[9] P. Cudazzo, I. V. Tokatly, and A. Rubio, Dielectric screening in two-dimensional insulators: implications for excitonic and impurity states in graphane, Phys. Rev. B **84,** 085406 (2011).

[10] T. C. Berkelbach, M. S. Hybertsen, and D. R. Reichman, Theory of neutral and charged excitons in monolayer transition metal dichalcogenides, Phys. Rev. B **88,** 045318 (2013).

[11] F. Hüser, T. Olsen, and K. S. Thygesen, How dielectric screening in two-dimensional crystals affects the convergence of excited-state calculations: monolayer MoS$_2$, Phys. Rev. B **88,** 245309 (2013).

[12] R. Soklaski, Y. Liang, and L. Yang, Temperature effect on optical spectra of monolayer molybdenum disulfide, Appl. Phys. Lett. **104,** 193110 (2014).

[13] A. Chernikov, T. C. Berkelbach, H. M. Hill, A. Rigosi, Y. Li, O. B. Aslan, D. R. Reichman, M. S. Hybertsen, and T. F. Heinz, Exciton Binding Energy and Nonhydrogenic Rydberg Series in Monolayer WS$_2$, Phys. Rev. Lett. **113,** 076802 (2014).

[14] D. Y. Qiu, F. H. da Jornada, and S. G. Louie, Optical Spectrum of MoS$_2$: Many-Body Effects and Diversity of Exciton States, Phys. Rev. Lett. **111,** 216805 (2013).

[15] D. Y. Qiu, F. H. da Jornada, and S. G. Louie, Optical Spectrum of MoS$_2$: Many-Body Effects and Diversity of Exciton States, Phys. Rev. Lett. **115,** 119901 (2015).

[16] S. Latini, T. Olsen, and K. S. Thygesen, Excitons in van der Waals heterostructures: The important role of dielectric screening, Phys. Rev. B **92,** 245123 (2015).

[17] D. Y. Qiu, F. H. da Jornada, and S. G. Louie, Screening and many-body effects in two-dimensional crystals: Monolayer MoS$_2$, Phys. Rev. B **93,** 235435 (2016).

[18] K. S. Thygesen, Calculating excitons, plasmons, and quasi-particles in 2D materials and van der Waals heterostructures, 2D Mater. **4**, 022004 (2017).

[19] W. Song and L. Yang, Quasiparticle band gaps and optical spectra of strained monolayer transition-metal dichalcogenides, Phys. Rev. B **96**, 235441 (2017).

[20] V. Tran, R. Soklaski, Y. Liang, and L. Yang, Layer-controlled band gap and anisotropic excitons in few-layer black phosphorus, Phys. Rev. B **89**, 235319 (2014).

[21] A. S. Rodin, A. Carvalho, and A. H. Castro Neto, Excitons in anisotropic two-dimensional semiconducting crystals, Phys. Rev. B **90**, 075429 (2014).

[22] V. Tran, R. Fei, and L. Yang, Quasiparticle energies, excitons, and optical spectra of few-layer black phosphorus, 2D Mater. **2**, 044014 (2015).

[23] R. Schuster, J. Trinckauf, C. Habenicht, M. Knupfer, and B. Büchner, Anisotropic Particle-Hole Excitations in Black Phosphorus, Phys. Rev. Lett. **115**, 026404 (2015).

[24] X. Wang, A. M. Jones, K. L. Seyler, V. Tran, Y. Jia, H. Zhao, H. Wang, L. Yang, X. Xu, and F. Xia, Highly anisotropic and robust excitons in monolayer black phosphorus, Nat. Nanotechnol. **10**, 517 (2015).

[25] H. Yuan, X. Liu, F. Afshinmanesh, W. Li, G. Xu, J. Sun, B. Lian, A. G. Curto, G. Ye, Y. Hikita, Z. Shen, S. C. Zhang, X. Chen, M. Brongersma, H. Y. Hwang, and Y. Cui, Polarization-sensitive broadband photodetector using a black phosphorus vertical p-n junction, Nat. Nanotechnol. **10**, 707 (2015).

[26] L. Li, J. Kim, C. Jin, G. J. Ye, D. Y. Qiu, F. H. da Jornada, Z. Shi, L. Chen, Z. Zhang, F. Yang, K. Watanabe, T. Taniguchi, W. Ren, S. G. Louie, X. H. Chen, Y. Zhang, and F. Wang, Direct observation of the layer-dependent electronic structure in phosphorene, Nat. Nanotechnol. **12**, 21 (2017).

[27] D. Y. Qiu, F. H. da Jornada, and S. G. Louie, Environmental screening effects in 2D materials: Renormalization of the bandgap, electronic structure, and optical spectra of few-layer black phosphorus, Nano Lett. **17**, 4706 (2017).

[28] Y. Chen and S. Y. Quek, Tunable bright interlayer excitons in few-layer black phosphorus based van der Waals heterostructures, 2D Mater. **5**, 045031 (2018).

[29] J. Zhou, T. Y. Cai, and S. Ju, Unusual Strain Dependence of Quasiparticle Electronic Structure, Exciton, and Optical Properties in Blue Phosphorene, Phys. Rev. Appl. **15**, 024045 (2021).

[30] J. Zhou, T. Y. Cai, and S. Ju, Quasiparticle band structure, exciton, and optical properties of few-layer blue phosphorus, Phys. Rev. B **104**, 245401 (2021).

[31] H. Thurn and H. Krebs, Über struktur und eigenschaften der halbmetalle. XXII. Die kristallstruktur des hittorfschen phosphors, Acta Cryst. B **25**, 125 (1969).

[32] L. Zhang, H. Huang, B. Zhang, M. Gu, D. Zhao, X. Zhao, L. Li, J. Zhou, K. Wu, Y. Cheng, and J. Zhang, Structure and properties of violet phosphorus and its phosphorene exfoliation, Angew. Chem. Int. Ed. **59**, 1074 (2020).

[33] A. G. Ricciardulli, Y. Wang, S. Yang, and P. Samorì, Two-dimensional violet phosphorus: A p-type semiconductor for (opto)electronics, J. Am. Chem. Soc. **144**, 3660 (2022).

[34] J. Zhou, T. Y. Cai, and S. Ju, Anisotropic exciton excitations and optical properties of Hittorf's phosphorene, Phys. Rev. Res. **2**, 033288 (2020).

[35] G. Shi and E. Kioupakis, Anisotropic spin transport and strong visible-light absorbance in few-layer SnSe and GeSe, Nano Lett. **15**, 6926 (2015).

[36] Y. H. Chan, D. Y. Qiu, F. H. da Jornada, and S. G. Louie, Giant exciton-enhanced shift currents and direct current conduction with subbandgap photo excitations produced by many-electron interactions, Proc. Natl. Acad. Sci. U.S.A. **118**, e1906938118 (2021).

[37] Z. Tang, G. J. Cruz, Y. Wu, W. Xia, F. Jia, W. Zhang, and P. Zhang, Giant Narrow-Band Optical Absorption and Distinctive Excitonic Structures of Monolayer C_3N and C_3B, Phys. Rev. Appl. **17**, 034068 (2022).

[38] L. V. Keldysh, The effect of a strong electric field on the optical properties of insulating crystals, JETP **34**, 788 (1958).

[39] L. V. Keldysh, Behavior of non-metallic crystals in strong electric fields, JETP **6**, 763 (1958).

[40] M. L. Cohen and S. G. Louie, *Fundamentals of Condensed Matter Physics* (Cambridge U.P., Cambridge, 2016).

[41] D. A. B. Miller, D. S. Chemla, T. C. Damen, A. C. Gossard, W. Wiegmann, T. H. Wood, and C. A. Burrus, Band-Edge Electroabsorption in Quantum Well Structures: The Quantum-Confined Stark Effect, Phys. Rev. Lett. **53**, 2173 (1984).

[42] D. A. B. Miller, D. S. Chemla, T. C. Damen, A. C. Gossard, W. Wiegmann, T. H. Wood, and C. A. Burrus, Electric field dependence of optical absorption near the band gap of quantum-well structures, Phys. Rev. B **32**, 1043 (1985).

[43] K. H. Khoo, M. S. C. Mazzoni, and S. G. Louie, Tuning the electronic properties of boron nitride nanotubes with transverse electric fields: A giant dc Stark effect, Phys. Rev. B **69**, 201401(R) (2004).

[44] M. Ishigami, J. D. Sau, S. Aloni, M. L. Cohen, and A. Zettl, Observation of the Giant Stark Effect in Boron-Nitride Nanotubes, Phys. Rev. Lett. **94**, 056804 (2005).

[45] V. Perebeinos and P. Avouris, Exciton ionization, Franz-Keldysh, and Stark effects in carbon nanotubes, Nano Lett. **7**, 609 (2007).

[46] C. H. Park and S. G. Louie, Energy gaps and Stark effect in boron nitride nanoribbons, Nano Lett. **8**, 2200 (2008).

[47] Y. Zhang, T. T. Tang, C. Girit, Z. Hao, M. C. Martin, A. Zettl, M. F. Crommie, Y. R. Shen, and F. Wang, Direct observation of a widely tunable bandgap in bilayer graphene, Nature **459**, 820 (2009).

[48] C. H. Park and S. G. Louie, Tunable excitons in biased bilayer graphene, Nano Lett. **10**, 426 (2010).

[49] E. J. Sie, J. W. Mclver, Y. H. Lee, L. Fu, J. Kong, and N. Gedik, Valley-selective optical Stark effect in monolayer WS_2, Nat. Mater. **14**, 290 (2015).

[50] J. Klein, J. Wierzbowski, A. Regler, J. Becker, F. Heimbach, K. Müller, M. Kaniber, and J. J. Finley, Stark effect spectroscopy of mono- and few-layer MoS_2, Nano Lett. **16**, 1554 (2016).

[51] S. Haastrup, S. Latini, K. Bolotin, and K. S. Thygesen, Stark shift and electric-field-induced dissociation of excitons in monolayer MoS_2 and BN/MoS_2 heterostructures, Phys. Rev. B **94**, 041401(R) (2016).

[52] B. Scharf, T. Frank, M. Gmitra, J. Fabian, I. Žutić, and V. Perebeinos, Excitonic Stark effect in MoS_2 monolayers, Phys. Rev. B **94,** 245434 (2016).

[53] C. Chakraborty, K. M. Goodfellow, S. Dhara, A. Yoshimura, V. Meunier, and A. N. Vamivakas, Quantum-confined Stark effect of individual defects in a van der Waals heterostructure, Nano Lett. **17,** 2253 (2017).

[54] X. Lu and L. Yang, Stark effect of doped two-dimensional transition metal dichalcogenides, Appl. Phys. Lett. **111,** 193104 (2017).

[55] J. G. Roch, N. Leisgang, G. Froehlicher, P. Makk, K. Watanabe, T. Taniguchi, C. Schönenberger, and R. J. Warburton, Quantum-confined Stark effect in a MoS_2 monolayer van der Waals heterostructure, Nano Lett. **18,** 1070 (2018).

[56] L. S. R. Cavalcante, D. R. da Costa, G. A. Farias, D. R. Reichman, and A. Chaves, Stark shift of excitons and trions in two-dimensional materials, Phys. Rev. B **98,** 245309 (2018).

[57] Z. Wang, Y. H. Chiu, K. Honz, K. F. Mak, and J. Shan, Electrical tuning of interlayer exciton gases in WSe_2 bilayers, Nano Lett. **18,** 137 (2018).

[58] M. Massicotte, F. Vialla, P. Schmidt, M. B. Lundeberg, S. Latini, S. Haastrup, M. Danovich, D. Davydovskaya, K. Watanabe, T. Taniguchi, V. I. Falko, K. S. Thygesen, T. G. Pedersen, and F. H. L. Koppens, Dissociation of two-dimensional excitons in monolayer WSe_2, Nat. Commun. **9,** 1633 (2018).

[59] H. C. Kamban and T. G. Pedersen, Field-induced dissociation of two-dimensional excitons in transition metal dichalcogenides, Phys. Rev. B **100,** 045307 (2019).

[60] I. Verzhbitskiy, D. Vella, K. Watanabe, T. Taniguchi, and G. Eda, Suppressed out-of-plane polarizability of free excitons in monolayer WSe_2, ACS Nano **13,** 3218 (2019).

[61] J. Pu, K. Matsuki, L. Chu, Y. Kobayashi, S. Sasaki, Y. Miyata, G. Eda, and T. Takenobu, Exciton polarization and renormalization effect for optical modulation in monolayer semiconductors, ACS Nano **13,** 9218 (2019).

[62] N. Leisgang, S. Shree, I. Paradisanos, L. Sponfeldner, C. Robert, D. Lagarde, A. Balocchi, K. Watanabe, T. Taniguchi, X. Marie, R. J. Warburton, I. C. Gerber, and B. Urbaszek, Giant Stark splitting of an exciton in bilayer MoS_2, Nat. Nanotechnol. **15,** 901 (2020).

[63] Y. Tang, J. Gu, S. Liu, K. Watanabe, T. Taniguchi, J. Hone, K. F. Mak, and J. Shan, Tuning layer-hybridized Moiré excitons by the quantum-confined Stark effect, Nat. Nanotechnol. **16,** 52 (2021).

[64] N. Abraham, K. Watanabe, T. Taniguchi, and K. Majumdar, Anomalous Stark shift of excitonic complexes in monolayer WS_2, Phys. Rev. B **103,** 075430 (2021).

[65] A. Chaves, T. Low, P. Avouris, D. Çakır, and F. M. Peeters, Anisotropic exciton Stark shift in black phosphorus, Phys. Rev. B **91,** 155311 (2015).

[66] T. Cao, Z. Li, D. Y. Qiu, and S. G. Louie, Gate switchable transport and optical anisotropy in $90°$ twisted bilayer black phosphorus, Nano Lett. **16,** 5542 (2016).

[67] Y. Liu, Z. Qiu, A. Carvalho, Y. Bao, H. Xu, S. J. R. Tan, W. Liu, A. H. Castro Neto, K. P. Loh, and J. Lu, Gate-tunable giant Stark effect in few-layer black phosphorus, Nano Lett. **17,** 1970 (2017).

[68] X. Chen, X. Lu, B. Deng, O. Sinai, Y. Shao, C. Li, S. Yuan, V. Tran, K. Watanabe, T. Taniguchi, D. Naveh, L. Yang, and F. Xia, Widely tunable black phosphorus mid-infrared photodetector, Nat. Commun. **8,** 1672 (2017).

[69] H. C. Kamban, T. G. Pedersen, and N. M. R. Peres, Anisotropic Stark shift, field-induced dissociation, and electroabsorption of excitons in phosphorene, Phys. Rev. B **102,** 115305 (2020).

[70] S. Yoon, T. Kim, S. Y. Seo, S. H. Shin, S. B. Song, B. J. Kim, K. Watanabe, T. Taniguchi, G. H. Lee, M. H. Jo, D. Y. Qiu, and J. Kim, Electrical control of anisotropic and tightly bound excitons in bilayer phosphorene, Phys. Rev. B **103,** L041407 (2021).

[71] P. Giannozzi, *et al.*, QUANTUM ESPRESSO: A modular and open-source software project for quantum simulations of materials, J. Phys.: Condens. Matter **21,** 395502 (2009).

[72] J. P. Perdew, K. Burke, and M. Ernzerhof, Generalized Gradient Approximation Made Simple, Phys. Rev. Lett. **77,** 3865 (1996).

[73] D. R. Hamann, Optimized norm-conserving Vanderbilt pseudopotentials, Phys. Rev. B **88,** 085117 (2013).

[74] M. S. Hybertsen and S. G. Louie, Electron correlation in semiconductors and insulators: Band gaps and quasiparticle energies, Phys. Rev. B **34,** 5390 (1986).

[75] M. Rohlfing and S. G. Louie, Electron-hole excitations and optical spectra from first principles, Phys. Rev. B **62,** 4927 (2000).

[76] J. Deslippe, G. Samzonidze, D. A. Strubbe, M. Jain, M. L. Cohen, and S. G. Louie, BerkeleyGW: A massively parallel computer package for the calculation of the quasiparticle and optical properties of materials and nanostructures, Comput. Phys. Commun. **183,** 1269 (2012).

[77] S. Ismail-Beigi, Truncation of periodic image interactions for confined systems, Phys. Rev. B **73,** 233103 (2006).

[78] B. C. Shih, Y. Xue, P. Zhang, M. L. Cohen, and S. G. Louie, Quasiparticle Band Gap of ZnO: High Accuracy from the Conventional G_0W_0 Approach, Phys. Rev. Lett. **105,** 146401 (2010).

[79] C. D. Spataru, S. Ismail-Beigi, R. B. Capaz, and S. G. Louie, Theory and *Ab Initio* Calculation of Radiative Lifetime of Excitons in Semiconducting Carbon Nanotubes, Phys. Rev. Lett. **95,** 247402 (2005).

[80] M. Palummo, M. Bernardi, and J. C. Grossman, Exciton radiative lifetimes in two-dimensional transition metal dichalcogenides, Nano Lett. **15,** 2794 (2015).

[81] B. Ghosh, S. Nahas, S. Bhowmick, and A. Agarwal, Electric field induced gap modification in ultrathin blue phosphorus, Phys. Rev. B **91,** 115433 (2015).

[82] C. Ke, Y. Wu, G. Y. Guo, W. Lin, Z. Wu, C. Zhou, and J. Kang, Tuning the Electronic, Optical, and Magnetic Properties of Monolayer GaSe with a Vertical Electric Field, Phys. Rev. Appl. **9,** 044029 (2018).

[83] Wikipedia, Quantum-confined Stark effect, https://en.wikipedia.org/wiki/Quantum-confined_Stark_effect.

[84] Y. H. Kuo, Y. K. Lee, Y. Ge, S. Ren, J. E. Roth, T. I. Kamins, D. A. B. Miller, and J. S. Harris, Strong quantum-confined Stark effect in germanium quantum-well structures on silicon, Nature **437,** 1334 (2005).

[85] Z. Sun, A. Martinez, and F. Wang, Optical modulators with 2D layered materials, Nat. Photonics **10,** 227 (2016).

[86] M. Liu, X. Yin, E. Ulin-Avila, B. Geng, T. Zentgraf, L. Ju, F. Wang, and X. Zhang, A graphene-based broadband optical modulator, Nature **474,** 64 (2011).

[87] E. O. Polat and C. Kocabas, Broadband optical modulators based on graphene supercapacitors, Nano Lett. **13,** 5851 (2013).

[88] N. Nikolay, N. Mendelson, N. Sadzak, F. Böhm, T. T. Tran, B. Sontheimer, I. Aharonovich, and O. Benson, Very Large and Reversible Stark-Shift Tuning of Single Emitters in Layered Hexagonal Boron Nitride, Phys. Rev. Appl. **11,** 041001(R) (2019).

[89] M. M. R. Adnan, D. Verma, Z. Xia, N. K. Kalarickal, S. Rajan, and R. C. Myers, Spectral Measurement of the Breakdown Limit of β-Ga$_2$O$_3$ and Tunnel Ionization of Self-Trapped Excitons and Holes, Phys. Rev. Appl. **16,** 034011 (2021).